Strain-induced bent domains in ferroelectric nitrides

Zhijun Jiang,[1,2,*] Zhenlong Zhang,[1] Charles Paillard,[3,4] Hongjun Xiang,[5,†] and Laurent Bellaiche[3,6,‡]

[1]*Ministry of Education Key Laboratory for Nonequilibrium Synthesis and Modulation of Condensed Matter, Shaanxi Province Key Laboratory of Advanced Functional Materials and Mesoscopic Physics, School of Physics, Xi'an Jiaotong University, Xi'an 710049, China*

[2]*State Key Laboratory of Surface Physics and Department of Physics, Fudan University, Shanghai 200433, China*

[3]*Smart Ferroic Materials Center, Physics Department and Institute for Nanoscience and Engineering, University of Arkansas, Fayetteville, Arkansas 72701, USA*

[4]*Université Paris-Saclay, CentraleSupélec, CNRS, Laboratoire SPMS, 91190 Gif-sur-Yvette, France*

[5]*Key Laboratory of Computational Physical Sciences (Ministry of Education), Institute of Computational Physical Sciences, State Key Laboratory of Surface Physics and Department of Physics, Fudan University, Shanghai 200433, China*

[6]*Department of Materials Science and Engineering, Tel Aviv University, Ramat Aviv, Tel Aviv 6997801, Israel*

(Received 2 June 2024; revised 10 July 2024; accepted 12 July 2024; published 5 August 2024)

Ferroelectric nitrides have emerged as promising semiconductor materials for modern electronics. However, their domain structures and associated properties are basically unknown, despite their potential to result in optimized or new phenomena. Density functional theory calculations are performed to investigate the effect of epitaxial strain on multidomains of (Al, Sc)N nitride systems and to compare it with the monodomain case. The multidomain systems are predicted to have five strain-induced regions, to be denoted as Regions I to V, respectively. Each of these regions is associated with rather different values or behaviors of physical properties such as axial ratio, polarizations, internal parameters, bond lengths, etc. Of particular interest is the prediction of bent domains under compressive strain extending beyond −5.5%, which indicates that domain walls may play a key role in the mechanical failure properties of these systems. Interestingly, such bending induces the creation of a finite in-plane polarization (in addition to out-of-plane dipoles) due to geometric and symmetry considerations. Strikingly too, the bent domains have lower energy than the wurtzite monodomains and have atomically sharp boundaries. Our findings may pave the way for domain-wall engineering in ferroelectric nitrides.

DOI: 10.1103/PhysRevB.110.054101

I. INTRODUCTION

Wurtzite AlN is a pyroelectric material but is not ferroelectric since its polarization direction cannot be switched by an electric field [1,2], which limits its applications [3,4]. On the other hand, new wurtzite-type ferroelectrics have been achieved by doping it with Sc to make $Al_{1-x}Sc_xN$ compounds [5], for which the polarization-*versus*-electric field hysteresis loops were observed for different Sc compositions. Such promising nitride system for technological applications [6,7] has therefore attracted great attention. In particular, its spontaneous polarization, that lies along the z axis, can be larger than 1.0 C/m^2, enabling applications for random access memories, actuators, and sensors [8–16].

Numerous theoretical studies have also been conducted in (Al,Sc)N alloys [17–22] and AlN/ScN superlattices [23–26], to explain the origin of the ferroelectricity, as well as to predict and understand other physical properties, including piezoelectricity, electro-optic conversion, and energy storage. Of particular importance for these properties is the existence of a nonpolar metastable hexagonal phase in ScN [27,28] and the possibility to continuously go from such nonpolar state to the wurtzite structure via a physical handle, which may be epitaxial strain or composition.

Moreover, ferroelectric materials typically exhibit domains, which are regions of uniform polarization usually forming during the paraelectric-to-ferroelectric phase transition [29]. The resulting domain wall separating two domains can adopt novel or enhanced characteristics, such as photovoltaic effects [30], electronic conductivity at ferroelectric domain walls [31,32], and strong magnetoresistance in $BiFeO_3$ domain walls [33], some of which are potentially mediated by the attraction of defects by the domain wall [34,35]. All these singular, localized, properties are expected to lead to novel applications in nanoelectronics [36]. To the best of our knowledge, domains and their possible evolutions with epitaxial strains are not well known in (Al, Sc)N systems. One may in fact wonder if surprises are in store there, especially when also realizing that polarization switching was found to occur via a novel mechanism in nitride ferroelectrics [37,38].

In the present study, we conduct first-principles calculations to investigate the evolution of strain-induced properties in multidomains and monodomains made of AlN/ScN superlattices. We do reveal the existence of unusual features, including multidomains that (1) are bent and that give rise to an additional in-plane polarization, that superimposes on typical out-of-plane dipoles; and (2) have atomically sharp domain walls.

This article is organized as follows: Section II provides details about the methods. Section III presents properties of the multidomain and monodomain. Finally, Sec. IV gives a summary of this work.

*Contact author: zjjiang@xjtu.edu.cn
†Contact author: hxiang@fudan.edu.cn
‡Contact author: laurent@uark.edu

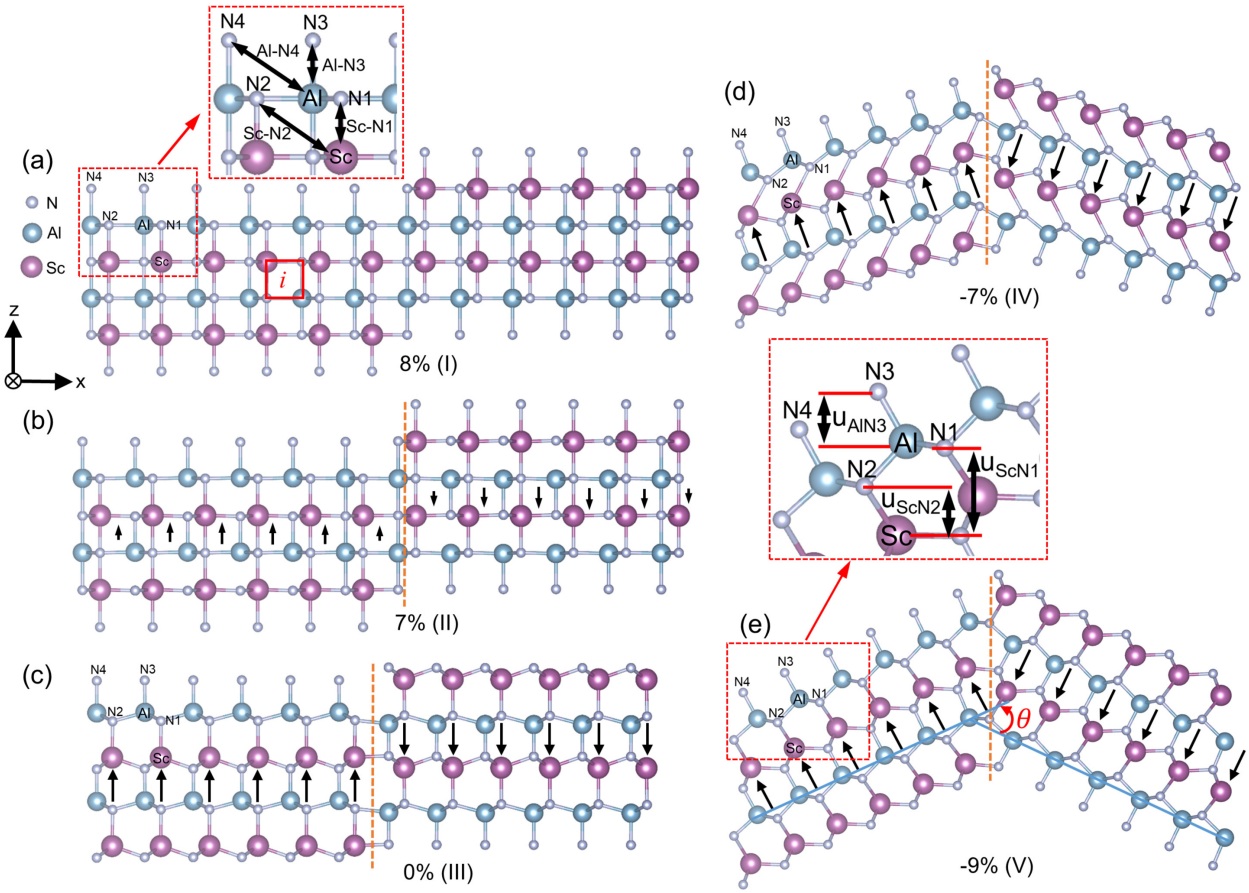

FIG. 1. Crystal structures of AlN/ScN superlattices. Panel (a) depicts the nonpolar hexagonal-derived structure in Region I for an epitaxial strain being equal to +8% (the red solid box defines a unit cell at number *i*). Panel (b) shows an intermediate multidomain structure of Region II for strain at +7%. Panel (c) displays a wurtzite-derived multidomain configuration in Region III for $\eta_{in} = 0\%$. Panel (d) shows the multidomain structure at −7% strain in Region IV. Panel (e) depicts the multidomain structure at −9% strain in Region V. The arrows represent the direction of the electric dipoles. The orange dashed lines represent the position of the domain walls. The bond lengths Sc-N1, Sc-N2, Al-N3, and Al-N4, internal parameters u_{ScN1}, u_{ScN2}, and u_{AlN3}, and the definition of the angle θ are shown in panels (a) and (e) and their inset.

II. METHODS

Two types of 1 × 1 AlN/ScN superlattices structures are initially considered in the present study. One is a wurtzite monodomain with a spontaneous polarization along the z direction. The other one is a wurtzite multidomain with 180° uncharged domain walls. Practically, the periodic supercell of the multidomain structure consists of two domains separated by two domain walls. As illustrated in Fig. 1(c), the polarization in the left and right domains in the initial multidomain structure is along the $+z$ and $-z$ direction of the supercell, respectively. These two supercells contain 12 × 1 × 2 unit cells that possess 96 atoms and that are periodic along the x, y, and z axes. Note that head-to-head and tail-to-tail domain structures are, in the absence of free carriers to screen the polarization bound charges, unstable in 1 × 1 AlN/ScN superlattices.

First-principles calculations are performed on the multidomain and monodomain structures based on density functional theory (DFT) with the generalized gradient approximation of the Perdew-Burke-Ernzerhof (PBE) exchange-correlation functional form [39], using the Vienna *ab initio* simulation package (VASP) [40,41]. The projector augmented-wave (PAW) method [42] implemented in VASP is employed to treat the interaction between core and valence electrons. A Γ-centered 1 × 11 × 3 k-point mesh is used to sample the Brillouin zone of the multidomain and monodomain and a plane-wave cutoff of 500 eV is adopted for all calculations. Different in-plane lattice constants a are chosen and then kept fixed while the out-of-plane lattice vector is allowed to relax in the simulations, and the atomic positions are fully optimized until the ionic forces are less than 0.001 eV/Å. The epitaxial strain is defined as $\eta_{in} = (a - a_{eq})/a_{eq}$, where a_{eq} is the in-plane lattice constant corresponding to the *equilibrium* structure of the monodomain in AlN/ScN superlattices, contrary to Ref. [24] that chose the hexagonal nonpolar structure as the reference for 0% strain. In the present study, the considered resulting strains are ranging between −10% and +10%. Note that an epitaxial compressive strain of about −7% and a tensile strain exceeding +8% were experimentally realized in $BiFeO_3$ thin films [43,44] and $La_{0.7}Ca_{0.3}MnO_3$ membranes [45]. Note also that our monodomain relaxed structure is in good agreement with previous theoretical results [23]. For completeness, we also considered rocksalt and zincblende structures with chemical ordering along the [111] cubic direction [see Fig. S1 of the Supplemental Material (SM) [46]].

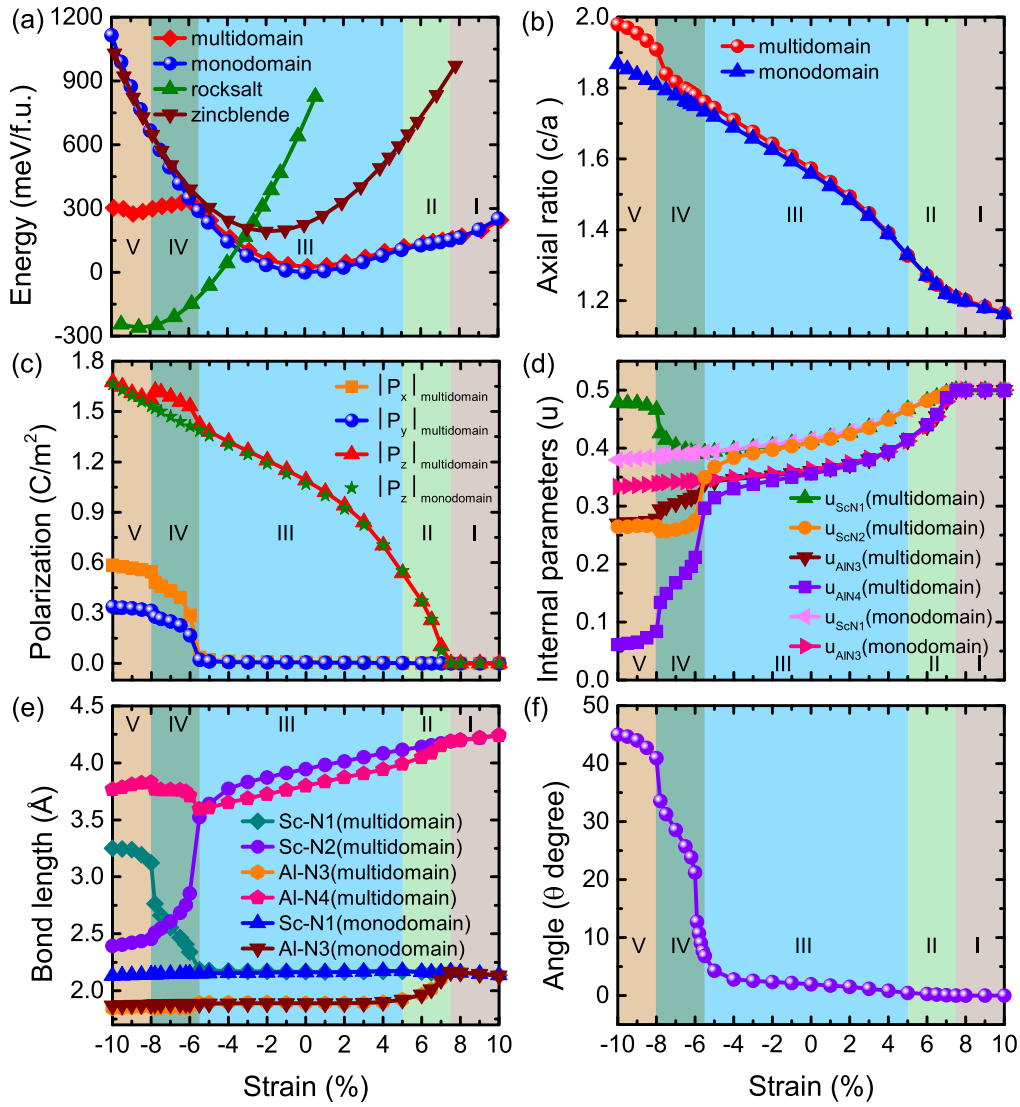

FIG. 2. Structural properties of AlN/ScN superlattices as a function of strain, for strains ranging between −10% and +10%. (a) The total energy of multidomain, monodomain, rocksalt, and zincblende structures in 1 × 1 AlN/ScN superlattices. (b) Axial ratio c/a of multidomain and monodomain. (c) The average of magnitude of the polarization in multidomain and monodomain; (d) Internal parameters u_{ScN} (including u_{ScN1} and u_{ScN2}) and u_{AlN} (including u_{AlN3} and u_{AlN4}) of multidomain and monodomain in AlN/ScN superlattices, respectively. (e) Bond lengths of Sc-N (including Sc-N1 and Sc-N2) and Al-N (including Al-N3 and Al-N4) in multidomain and monodomain. (f) Angle θ of multidomain.

III. RESULTS AND DISCUSSION

A. Structural properties in multidomain and monodomain

Figures 1(a)–1(e) show the relaxed crystal structures of the multidomain for different strains. Moreover, Figs. 2(a)–2(e) display different properties of both the multidomain and monodomain as a function of strain, which are the total energy (per unit cell) in our considered AlN/ScN superlattices; the c/a axial ratio; the supercell averaged *magnitude* of the three Cartesian components of the local polarization ($|P_x|$, $|P_y|$, and $|P_z|$, where $|P_\alpha| = \sum_i |P_{i,\alpha}|/N$, where $\alpha = x, y,$ or z and where i runs over all the N unit cell of the supercells); different internal parameters u_{ScN} (respectively, u_{AlN}) connecting the relative position along the z axis of Sc (respectively, Al) and some N atoms [see Fig. 1(e)]; and bond lengths between Sc and different N atoms, as well as between Al and various N atoms [see Fig. 1(a)]. Furthermore, Fig. 2(f) shows the θ angle that is depicted in Fig. 1(e), and that is related to the deviation of atomic lines from horizontality between the two domains in the relaxed multidomain configuration. The strain-induced behaviors of the properties for the multidomain case displayed in Fig. 2 allow the determination of five different strain regions, that we denote as Regions I to V, respectively.

Region I occurs for tensile strain larger than +7.5% and corresponds to a layered *nonpolar* hexagonal-derived structure, as evinced by c/a being close to 1.2, $|P_x| = |P_y| = |P_z|$ being zero and the internal parameters being equal to 0.5, as shown in Figs. 2(b)–2(d), respectively. Note that the phase in Region I has the nonpolar $P\bar{6}m2$ space group for both the multidomain and monodomain that have similar structure [see an example of this structure in Fig. 1(a)], which also explains why the total energies and c/a axial ratio of the multidomain and monodomain cases are basically identical there. The Sc-N1 and Al-N3 bond lengths of Fig. 2(e) are equal to each other

and very slightly increase with strain from 2.14 to 2.17 Å for strains decreasing between +10% and +7.5%. Similarly, the Sc-N2 and Al-N4 bond lengths, while also equal to each other, decrease with strain (from 4.24 to 4.19 Å) in Region I. Figure 2(f) indicates that the angle θ, which describes how the two domains are bent, is null in the entire Region I, as consistent with the nonpolar hexagonal-derived phase.

The next region, that is, Region II, pertains to strain ranging between +7.5% and +5%. It has the polar $Pmc2_1$ space group for the multidomain *versus* polar $P3m1$ for the monodomain. It is characterized by the occurrence of a polarization aligned parallel or antiparallel to the z axis in each domain in the multidomain (while the polarization is only along $+z$ in the monodomain case), with $|P_z|$ rapidly increasing from zero to 0.54 C/m^2 when the strain decreases—as shown in Fig. 2(c). The c/a axial ratio concomitantly increases from 1.21 to 1.33 in both the multidomain and monodomain. Meanwhile, the internal parameters u_{AlN3} and u_{AlN4} of the multidomain both decrease from 0.5 to 0.41 when reducing the strain from +7.5% to +5% in Region II, and are now distinct from $u_{\mathrm{ScN1}} = u_{\mathrm{ScN2}}$ of the multidomain—with $u_{\mathrm{ScN1}} = u_{\mathrm{ScN2}}$ decreasing from 0.5 to 0.47. Concurrently, the Al-N3 bond length decreases from 2.17 to 1.92 Å while that of Sc-N1 remains constant and close to 2.17 Å. Moreover, the bond lengths of Sc-N2 (from 4.19 to 4.11 Å) and Al-N4 (from 4.19 to 3.99 Å) begin to be distinct from each other and both decrease with strain when the tensile strain reduces in Region II. Interestingly, the angle θ starts to very slightly deviates from zero and weakly increases from 0 to 0.5 degrees. Note that the behaviors of the total energy, c/a, $|P_z|$, internal parameters, and bond lengths of the monodomain are very close to those of the multidomain in Region II [see Figs. 2(a)-2(e)]. Structurally, Region II shows in Fig. 1(b), both for the monodomain supercell and the domains of the multidomain, a phase that is in-between the hexagonal-derived nonpolar structure [see Fig. 1(a)] and the wurtzite-derived structure [see Fig. 1(c)].

Region III possesses a strain ranging from +5% to −5.5%. As in Region II, it holds a $Pmc2_1$ space group for the multidomain and $P3m1$ for the monodomain. It has very small in-plane polarization components $|P_x|$ and $|P_y|$ (close to zero), while $|P_z|$ is still nonzero [see Fig. 2(c)] (as in the ideal wurtzite structure) and increases when decreasing the strain. The c/a axial ratio strengthens from 1.33 to 1.76 for the multidomain (respectively, from 1.33 to 1.73 for the monodomain) when the strain varies from +5% to −5.5%. The internal parameters remain equal to each other in the multidomain and monodomain cases, with the exception of u_{ScN2} and u_{AlN4} close to −5.5% strain (note that $u_{\mathrm{ScN2}} = u_{\mathrm{ScN1}}$ and $u_{\mathrm{AlN4}} = u_{\mathrm{AlN3}}$ in the monodomain). All internal parameters decrease when going toward more compressive strain within Region III. The θ angle slightly increases from 0.5 to 2.7 degrees, making the two corresponding atomic lines bend more and more from each other, when decreasing the strain from +5% to −4%. It then rapidly increases from 2.7 to 6.8 degrees for strains varying between −4% and −5.5%. The behavior of the internal parameters coupled with that of the θ angle in Region III make the Sc-N1 and Al-N3 bond lengths almost constant (around 2.17 and 1.89 Å for Sc-N1 and Al-N3, respectively) in the multidomain case. Note that Regions II and III are distinct from each other due to the bond length of Al-N3 significantly decreasing with strain in Region II while being basically a constant in Region III. The Sc-N2 and Al-N4 bond lengths decrease significantly from 4.12 to 3.53 Å and from 3.99 to 3.59 Å, respectively, in Region III for the multidomain case, because N2 and N4 atoms are moving toward Sc and Al atoms, respectively, when the compressive strain strengthens in magnitude. Structurally speaking, each domain in the multidomain case (as well as the monodomain) corresponds to a wurtzite-derived phase in Region III. Note that, in Region III, the total energy of the multidomain remains higher than that of the monodomain, as expected. As indicated above, the c/a axial ratio, $|P_z|$, internal parameters, and bond lengths of the monodomain are very close to the multidomain case in Region III, with the exception of Sc-N2 and Al-N4 at the boundary of −5.5% (not shown here). Note also that the system found a minimum in energy in Region III for both the multidomain and monodomain for 0% of epitaxial strain, while characteristics of the ideal wurtzite structure (namely, c/a close to 1.633 and the internal parameter averaged between u_{ScN1} and u_{AlN3} being around 0.375) occur for a strain around −2.3% for both the multidomain and monodomain supercells.

Moreover, Region IV extends from −5.5% to −8%. Strikingly, the total energy of the multidomain in this region has now a lower energy than the wurtzite-like monodomain, implying that the multidomain adopts a configuration that is more stable here. The c/a axial ratio is much larger than that of the ideal wurtzite structure (which is 1.633) and varies from 1.76 to 1.91 for strain ranging between −5.5% and −8% in the multidomain (c/a increases from 1.73 to 1.82 for the monodomain case). Remarkably, the electric dipoles are tilted away from the [0001] direction (z axis) of the ideal wurtzite structure in each domain of the multidomain case, while the dipoles of the monodomain are still all along the z axis (as in the wurtzite structure). Consequently, the multidomain now possesses both finite $|P_x|$, $|P_y|$, in addition to significant $|P_z|$. All these three components increase when strengthening the magnitude of the compressive strain. In the multidomain, the internal parameter u_{ScN1} increases with the magnitude of strain while u_{ScN2}, u_{AlN3}, and u_{AlN4} decrease. These features are due to the fact that the N1 atom is moving away from Sc while the N2, N3, and N4 atoms are gradually approaching Sc and Al atoms, respectively [see an example of this structure in Fig. 1(d)]. Note that, in contrast, the internal parameters of the monodomain all linearly decrease with strain for that range [see Fig. 2(d)]. The internal parameters of the multidomain are thus markedly different from those of the monodomain in Region IV. The aforementioned motions of the N2 and N4 atoms results in the Sc-N2 bond length decreasing significantly from 3.53 to 2.45 Å while Al-N4 slightly increases from 3.59 to 3.83 Å in Region IV for the multidomain. Furthermore, for the multidomain, the Sc-N1 bond length dramatically increases from 2.18 to 3.12 Å when increasing the magnitude of the compressive strain in Region IV [see Fig. 2(e)], which is due to the combined behavior of c/a and the internal parameter u_{ScN1}. The Sc-N2 bond length then becomes smaller than that of Sc-N1 for some strains in Region IV. Furthermore, the angle θ significantly increases from 6.8 to 33.5 degrees when increasing the amount of compressive strain in Region

IV, revealing that atomic lines between the two domains are strongly bent with respect to each other [see Fig. 1(d)]. In effect, one Sc atomic layer appears to slide to allow a reconfiguration of the atomic bonding within the domain walls with large compressive strain [compare Fig. 1(d) with Fig. 1(e)]. Region IV thus acts as a transition region through which Sc atoms are breaking their bond with N1 to create a new bond with N2. The stress-strain curve (see Fig. S2 of the SM [46]) shows that the multidomain structure in-plane stress exhibits a sharp fall, typical of mechanical failure calculated for instance in nitride monolayers [47,48] and here occurring at -5.5% critical strain. There is thus a strong possibility that domain walls lower the ability of ferroelectric nitrides to sustain large elastic deformations. It is interesting to realize that the bending between two domains was also experimentally and recently found in two-dimensional (2D) van der Waals ferroelectrics such as the α-In_2Se_3 material [49], with a bending angle θ above $\approx$33 degrees. Note that $|P_x|$ likely naturally results from the geometrical bending occurring the (x, z) plane. Mirror symmetry imposed by the $Pmc2_1$ space group further imposes the appearance of $|P_y|$, with the constraint that P_y equals to $P_x/\sqrt{3}$, as demonstrated in Fig. S3 of the SM [46]. Moreover, the structure in each domain of the multidomain corresponds to a distorted-pyramidal structure because the Sc-N1 and Sc-N2 bond lengths are very different from those in the case of the wurtzite configuration. Note that the overall phase in Region IV retains the $Pmc2_1$ space group for the multidomain while the monodomain also keeps its $P3m1$ space group, as in Regions II and III.

Finally, Region V occurs for strains ranging between -8% and -10%, with the multidomain and monodomain also preserving their $Pmc2_1$ and $P3m1$ space group, respectively. The multidomain has now a much lower energy than the monodomain [see Fig. 2(a)]. The boundary between Regions IV and V occurs at a strain of $\approx -8\%$, where the axial ratio c/a, the three components of the polarization, internal parameters, bond lengths, and angle θ of the multidomain all experience a significant jump. These jumps, as well as the retaining of the $Pmc2_1$ space group, characterize a strain-induced first-order *isostructural* transition in the multidomain supercell (see Refs. [50,51] and references therein). The resulting structure in each domain is a pyramidal structure [see Fig. 1(e)]. The overall structure in Region V [see Fig. 1(e)] differs from Region IV [see Fig. 1(d)] because the c/a, internal parameters, bond lengths, and angle θ are very different in these two regions in the more stable multidomain supercell. As a matter of fact, Fig. 2(b) shows that the c/a axial ratio of the multidomain is extremely large, and larger than that of the monodomain in Region V. It nearly linearly increases from 1.91 to 1.98 when strengthening the magnitude of the compressive strain. The angle θ concomitantly nonlinearly increases with strain, adopting enormous values ranging from 40.9 to 45.0 degrees. Consequently, $|P_x|$ (from 0.55 to 0.59 C/m^2) and $|P_y|$ (from 0.31 to 0.34 C/m^2) all increase nearly linearly with strain for the multidomain. $|P_z|$ also increases from 1.57 to 1.67 C/m^2 in the multidomain (to be compared from 1.53 to 1.66 C/m^2 for the monodomain) as a response to in-plane compressive strain becoming bigger in magnitude. Furthermore, the internal parameter u_{ScN1} of the multidomain increases with strain as well (from 0.466 to 0.478) while u_{AlN3} concomitantly slightly decreases (from 0.278 to 0.270) in Region V. u_{ScN2} and u_{AlN4} of the multidomain also slightly decrease from 0.266 to 0.265 and from 0.066 to 0.061, respectively, in Region V. Note that u_{AlN4} is really small, indicating that the z component of the N4 atomic position is very close to that of the Al atom in Region V. Figure 2(e) shows that the bond length of Sc-N1 and Al-N3 slightly increases (from 3.12 to 3.25 Å) and decreases (from 1.86 to 1.84 Å) with strain, respectively, in Region V for the multidomain (the bond length of Sc-N2 and Al-N4 linearly decreases from 2.45 to 2.39 and from 3.83 to 3.77 Å, respectively). Note that the c/a, polarization, internal parameters, and bond lengths behaviors of the monodomain are very different from those of the multidomain case in Region V because the monodomain is wurtzite-like while it is a pyramidal structure for each domain of the multidomain. Note also that the total energy of the multidomain has a slight minimum around -9%. The multidomain therefore adopts a metastable state around -9%, in addition to its wurtzite-like ground state for 0% strain. Such features bear resemblance with $BiFeO_3$ films, that possess two polymorphs, usually denoted as the T and R phases, with minima located at very different strains [52]. It is also worth noting that the SM [46] indicates that the stress-strain curves in Region V recover a linear dependency, indicative of an elastic deformation regime.

B. Local polarizations in multidomain and monodomain

Let us now present the evolution of the polarization *plane-by-plane* for Regions II, III, IV, and V in the multidomain case, and also compare it with the monodomain case. The local polarization in the unit cell i [as shown in Fig. 1(a) by the solid box] is computed via $\mathbf{p}^i = \frac{e}{\Omega}\sum_j Z_j^* \mathbf{u}_j$ [53,54], where e is the electron charge, Ω is the unit-cell volume, Z_j^* is the Born effective charge tensor, and $\mathbf{u}_j$ is the atomic displacement from the ideal lattice site of ion j—with j running over all atoms in the unit cell i. Note that Fig. 2(c) displays the averaged *magnitude* of components of the local polarization, $|P_x|$, $|P_y|$, $|P_z|$, while Fig. 3 characterizes *components* of the plane-by-plane polarizations p_x, p_y, p_z, that are along the x, y, and z axes, respectively. In particular, only p_z is finite in the monodomain and it is homogeneous for all Regions II–V. Figure 3 indicates that p_z *averaged over the entire supercell* is always zero in the multidomain for all regions because of the opposite directions of the local out-of-plane polarization in the two domains. Note also that we do not show the local polarization distributions in Region I since the phase there is nonpolar because of its hexagonal-derived structure [see Fig. 1(a)].

As representative of Region II, we chose a strain of $+7\%$. Figure 3(a) shows that the polarization p_z in the multidomain behaves like a sine function along the x direction, changing signs between the two domains and generating smooth waves of polarization in Region II. This is characteristic of an Ising-like feature [55] for the behavior of p_z. In comparison, in the monodomain, the local polarization p_z is uniform along the x direction and equal to 0.075 C/m^2. This value is smaller in magnitude than that of the p_z of the multidomain for cell numbers ranging from 2 to 5 and from 8 to 11, respectively.

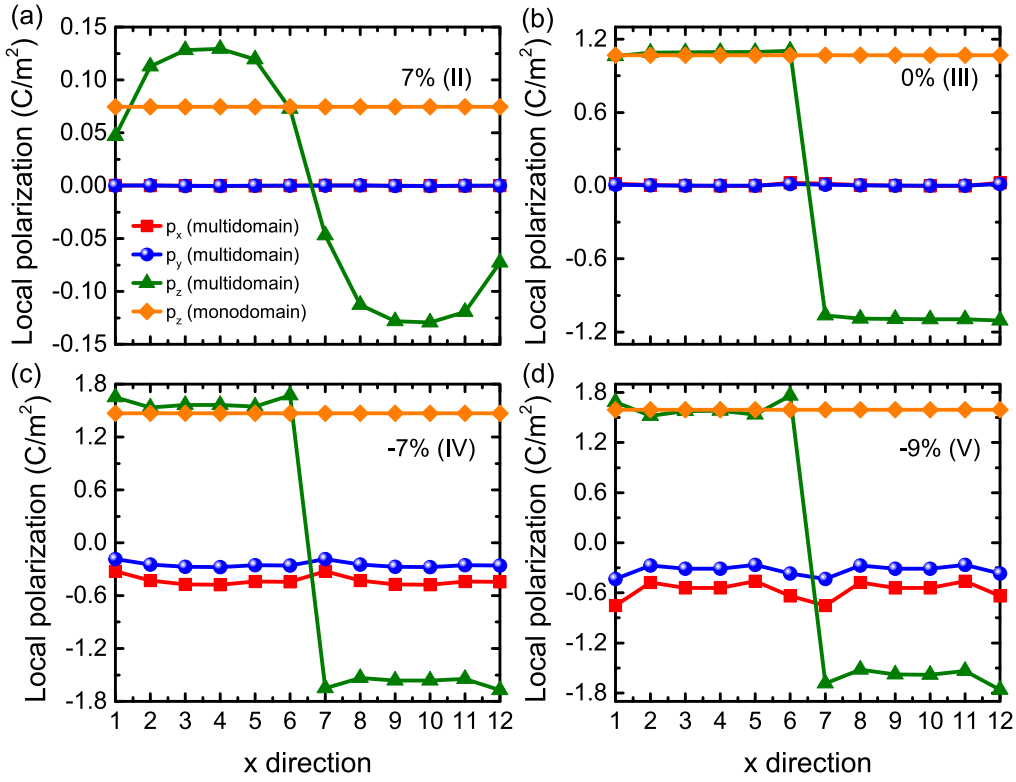

FIG. 3. The local x, y, z components of polarizations in each unit cell along the x-axis direction for different strains at (a) 7% (Region II), (b) 0% (Region III), (c) −7% (Region IV), and (d) −9% (Region V) in the multidomain and monodomain cases of AlN/ScN superlattices, respectively.

On the other hand, it is larger in magnitude than the p_z of the multidomain for cell numbers 1 and 7. Interestingly, the magnitude of p_z in the multidomain at cell numbers 6 and 12 (located in the vicinity of the domain wall) is very close to that of the monodomain. These behaviors make the averaged magnitude $|P_z|$ of the multidomain and monodomain being equal to each other, as shown in Fig. 2(c) for Region II. Note that the local in-plane polarizations, p_x and p_y, are null at any cell in the multidomain in Region II.

We now chose 0% of strain as a representative of Region III. Figure 3(b) shows that p_z in each domain of the multidomain is almost constant in magnitude along the x direction and equal to ≈1.1 C/m^2. This p_z thus appears to behave like a square wave, because of its change of sign between the two domains, and is equal in magnitude to the p_z of the monodomain case [see Fig. 3(b)]. It is striking to thus realize that there is a sudden jump between the p_z of the two different domains, implying that the domain wall can be extremely small in this system. This dramatically contrasts with the case of 90° domain walls in ferroelectric perovskites and domain walls in magnetic systems for which they can extend over a length of typically 15 and 500 nm, respectively [56,57]. These characteristics also make the $|P_z|$ of the multidomain and monodomain essentially equal to each other in Region III [see Fig. 2(c)]. Moreover and as shown in Fig. 3(b), p_x and p_y continue to vanish in Region III for the multidomain and monodomain.

In Region IV, for which we use a representative strain of −7%, Fig. 3(c) displays a large value in magnitude for p_z (≈1.59 C/m^2) in the entire multidomain. This p_z also behaves as a square wave, with a sudden jump between the two domains and forms a sharp domain wall (note that the bent domains experimentally found in α-In_2Se_3 material are also sharp and can be extremely narrow, down to two atoms or 4 Å wide at their narrowest point [49]). Furthermore, the p_z on the monodomain continues to be homogeneous and is now equal to 1.47 C/m^2, which is smaller in magnitude than in the multidomain (≈1.59 C/m^2). Consequently, the $|P_z|$ in the multidomain is larger than in the monodomain in Region IV, as shown in Fig. 2(c). Interesting, Fig. 3(c) reveals that the in-plane p_x and p_y are no longer null in Region IV. They are quasihomogeneous ($p_x \approx -0.43$ C/m^2 and $p_y \approx -0.25$ C/m^2, respectively). The homogeneity of p_x, including when going from one domain to another one, guarantees that the domains are uncharged.

Finally, we consider a large compressive strain of −9% for Region V. Figure 3(c) shows that p_z of the multidomain is nearly constant in each domain and displays a large value in magnitude around 1.61 C/m^2 for cell numbers ranging from 1 to 12, which is very close to that of the monodomain (1.6 C/m^2). Therefore, the $|P_z|$ in the multidomain and monodomain are nearly equal to each other, as displayed in Region V of Fig. 2(c). Once again, the domain walls are sharp for p_z in the multidomain as they present a sudden jump from a large positive value to its opposite when going from the left domain to the right one. Moreover, p_x and p_y are nonzero and quasihomogeneous as well in Region V, albeit with a larger in magnitude than in Region IV (p_x is now around −0.6 C/m^2 and p_y around −0.3 C/m^2 at −9% strain, respectively) for the multidomain. Note that the near continuity of p_x across

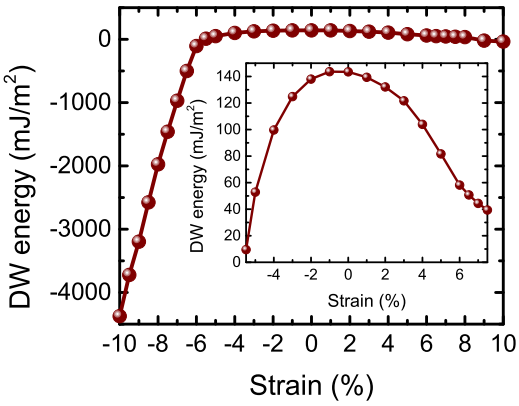

FIG. 4. Domain-wall energy in 1×1 AlN/ScN superlattices. The inset zooms in the data in Regions II and III.

the two domains implies that the domain walls in Region V remain uncharged.

C. Domain-wall energy and stability of the multidomain state

The domain-wall (DW) energy E_{DW} is computed by the equation [22,53,58]: $E_{\mathrm{DW}} = (E_{\mathrm{multi}} - E_{\mathrm{mono}})/2S_{\mathrm{DW}}$, where E_{multi} is the total energy of multidomain, E_{mono} is the total energy of monodomain, and S_{DW} is the area of the domain wall. Figure 4 shows the domain-wall energy as a function of strain. For strains ranging between $+7.5\%$ and $+10\%$ (Region I), the domain-wall energies are close to zero because both the multidomain and monodomain have a layered *nonpolar* hexagonal-derived structure there.

The monodomain polar state of 1×1 AlN/ScN superlattices is the most stable state in Regions II and III according to Fig. 2(a). In these regions, the domain-wall energy increases from almost zero (at the compressive edge of Region III) to 143 mJ/m^2 at zero strain (see the inset of Fig. 4). It then decreases again when one approaches the boundary between Regions II and I (nonpolar hexagonal phase). 180 degree domain walls in our AlN/ScN have thus a comparable surface energy compared with uniaxial ferroelectrics such as $PbTiO_3$, where energies of the order of 125 mJ/m^2 were reported [34,53]. Interestingly, both compressive and tensile strain tend to decrease the domain-wall surface energy, likely because phase transitions to centrosymmetric phases can be expected on both the compressive [transition to the rocksalt phase, see Fig. 2(a)] and tensile (transition to the nonpolar hexagonal phase [24]) side.

Interestingly, in the strongly compressive strain regime (Regions IV and V), the domain-wall energies become negative with values ranging from -107 to -4372 mJ/m^2. The negative domain-wall energies suggest that the bent multidomain state is more energetically favorable than the monodomain polar state, as consistent with Fig. 2(a). Interestingly, in Regions IV, where the multidomain state becomes energetically more favorable with respect to the monodomain state, marks the onset of mechanical failure, as strain-stress curves (see Fig. S2 of the SM [46]) show a strong drop in the longitudinal stress facilitated by the strong bending of the domains. Note, however, that elastic behavior is recovered in Region V, indicating that such bent multidomain state may be metastable at extremely large compressive strains.

One may wonder whether such bent multidomain state can be accessed experimentally. Figure 2(a) indicates that this peculiar state can in fact only be metastable in 1×1 AlN/ScN superlattices. Indeed, in Regions IV and V, the nonpolar rocksalt phase is numerically found to have lower energy by 300 to 600 meV/f.u. It is fairly evident that slowly applied strain, such as epitaxial strain resulting from growth of a thin film on a substrate, could not address this peculiar domain state. However, large, ultrafast strain pulses (such as the nondestructive laser shock technique developed in Ref. [59]) may be able to address such a metastable state by creating the necessary amount of deformation to cause mechanical failure and stabilize the bent domain state. Note also that over AlN/ScN superlattices, such as 3×1, possess a small stability window where the bent multidomain state is in fact found to be the ground state (see Fig. S4 of the SM [46] between -6% and -4% compressive strain). It is thus possible that altering the composition of the superlattice may reveal such original bent multidomain states.

IV. SUMMARY

In summary, based on *ab initio* density functional theory calculations, we predict the existence of five different strain regions, accompanied by striking structural features, in (uncharged) multidomains of AlN/ScN superlattices. In particular, for the largest studied tensile strains, Region I has no local polarization, while a polarization along $+z$ and $-z$ develops in each domain of such a multidomain, respectively, in Region II—that exists for smaller tensile strains and that possesses a sinusoidal behavior of its plane-by-plane polarization. The polarization in each of these domains, as well as the axial ratio, significantly grow when going from tensile to compressive strain in Region III, with the plane-by-plane polarization now exhibiting a square-like behavior.

Strikingly, these domains bend in Regions IV and V, with this bending becoming stronger as the compressive strain is enhanced in magnitude and with the transition from Regions IV to V being isostructural and of first order. Such binding results in the appearance of in-plane and homogeneous polarization. Remarkably, the 180° domain walls in Regions II to V are very sharp. Although these bent domains do not appear to be stable at thermodynamic equilibrium, it is possible that strong out-of-equilibrium excitations, such as large strain pulses, could access this peculiar state which has lower energy than the monodomain state under large compressive strain. Note that we also checked the properties of multidomains made of the epitaxial 3×1 AlN/ScN superlattices. They exhibit qualitatively similar results as the presently studied 1×1 AlN/ScN superlattices, in general, and possess bent domains too, in particular. Interestingly, these bent domains occur under smaller compressive strain for the 3×1 AlN/ScN superlattices, namely, around -4% (see Fig. S4 of the SM [46])—with these bent domains having even lower energy than the rocksalt and zinc-blende structures, as well as the wurtzite monodomain, for some strain range. In other words, bent domains can be the ground state in some cases, and the critical strain at which these intriguing bent domains

appear in ferroelectric nitrides depend on parameters, such as the overall composition or thickness layers—it is thus also possible that other superlattice compositions may be able to sustain such bent domains before the onset of the phase transition to the centrosymmetric rocksalt structure.

ACKNOWLEDGMENTS

This work is supported by the National Natural Science Foundation of China (Grant No. 12374092), Natural Science Basic Research Program of Shaanxi (Program No. 2023-JC-YB-017), Shaanxi Fundamental Science Research Project for Mathematics and Physics (Grant No. 22JSQ013), "Young Talent Support Plan" of Xi'an Jiaotong University (Grant No. WL6J004), the Open Project of State Key Laboratory of Surface Physics (Grant No. KF2023_06), the Fundamental Research Funds for the Central Universities, and the HPC Platform of Xi'an Jiaotong University. H.X. acknowledges financial support from the National Key R&D Program of China (No. 2022YFA1402901), NSFC (Grants No. 11991061 and No. 12188101), Shanghai Science and Technology Program (No. 23JC1400900), and the Guangdong Major Project of the Basic and Applied Basic Research (Future functional materials under extreme conditions–2021B0301030005). C.P. and L.B. thank the Defense Advanced Research Projects Agency Defense Sciences Office (DARPA-DSO) Program: Accelerating discovery of Tunable Optical Materials (ATOM) under Agreement No. HR00112390142 and the Award No. FA9550-23-1-0500 from the U.S. Department of Defense under the DEPSCoR program. C.P. acknowledges partial support through Agence Nationale de la Recherche through Grant Agreement No. ANR-21-CE24-0032 (SUPERSPIN). L.B. also acknowledges the MonArk NSF Quantum Foundry supported by the National Science Foundation Q-AMASE-i Program under NSF Award No. DMR-1906383, the ARO Grant No. W911NF-21–1–0113, and the Vannevar Bush Faculty Fellowship (VBFF) Grant No. N00014-20-1–2834 from the Department of Defense.

[1] A. F. Wright and J. S. Nelson, Consistent structural properties for AlN, GaN, and InN, Phys. Rev. B **51**, 7866 (1995).

[2] C. Bungaro, K. Rapcewicz, and J. Bernholc, *Ab initio* phonon dispersions of wurtzite AlN, GaN, and InN, Phys. Rev. B **61**, 6720 (2000).

[3] F. Bernardini, V. Fiorentini, and D. Vanderbilt, Spontaneous polarization and piezoelectric constants of III–V nitrides, Phys. Rev. B **56**, R10024(R) (1997).

[4] C. E. Dreyer, A. Janotti, C. G. Van de Walle, and D. Vanderbilt, Correct implementation of polarization constants in wurtzite materials and impact on III-nitrides, Phys. Rev. X **6**, 021038 (2016).

[5] S. Fichtner, N. Wolff, F. Lofink, L. Kienle, and B. Wagner, AlScN: A III-V semiconductor based ferroelectric, J. Appl. Phys. **125**, 114103 (2019).

[6] M. Dawber, K. M. Rabe, and J. F. Scott, Physics of thin-film ferroelectric oxides, Rev. Mod. Phys. **77**, 1083 (2005).

[7] J. F. Scott, Applications of modern ferroelectrics, Science **315**, 954 (2007).

[8] S. Yasuoka, T. Shimizu, A. Tateyama, M. Uehara, H. Yamada, M. Akiyama, Y. Hiranaga, Y. Cho, and H. Funakubo, Effects of deposition conditions on the ferroelectric properties of $(Al_{1-x}Sc_x)N$ thin films, J. Appl. Phys. **128**, 114103 (2020).

[9] K. Yazawa, D. Drury, A. Zakutayev, and G. L. Brennecka, Reduced coercive field in epitaxial thin film of ferroelectric wurtzite $Al_{0.7}Sc_{0.3}N$, Appl. Phys. Lett. **118**, 162903 (2021).

[10] N. Wolff, S. Fichtner, B. Haas, M. R. Islam, F. Niekiel, M. Kessel, O. Ambacher, C. Koch, B. Wagner, F. Lofink, and L. Kienle, Atomic scale confirmation of ferroelectric polarization inversion in wurtzite-type AlScN, J. Appl. Phys. **129**, 034103 (2021).

[11] P. Wang, D. Wang, N. M. Vu, T. Chiang, J. T. Heron, and Z. Mi, Fully epitaxial ferroelectric ScAlN grown by molecular beam epitaxy, Appl. Phys. Lett. **118**, 223504 (2021).

[12] S.-L. Tsai, T. Hoshii, H. Wakabayashi, K. Tsutsui, T.-K. Chung, E. Y. Chang, and K. Kakushima, Room-temperature deposition of a poling-free ferroelectric AlScN film by reactive sputtering, Appl. Phys. Lett. **118**, 082902 (2021).

[13] R. Guido, P. D. Lomenzo, M. R. Islam, N. Wolff, M. Gremmel, G. Schönweger, H. Kohlstedt, L. Kienle, T. Mikolajick, S. Fichtner, and U. Schroeder, Thermal stability of the ferroelectric properties in 100 nm-thick $Al_{0.72}Sc_{0.28}N$, ACS Appl. Mater. Interfaces **15**, 7030 (2023).

[14] D. Wang, P. Wang, S. Mondal, M. Hu, Y. Wu, T. Ma, and Z. Mi, Ultrathin nitride ferroic memory with large ON/OFF ratios for analog in-memory computing, Adv. Mater. **35**, 2210628 (2023).

[15] J. X. Zheng, M. M. A. Fiagbenu, G. Esteves, P. Musavigharavi, A. Gunda, D. Jariwala, E. A. Stach, and R. H. Olsson III, Ferroelectric behavior of sputter deposited $Al_{0.72}Sc_{0.28}N$ approaching 5 nm thickness, Appl. Phys. Lett. **122**, 222901 (2023).

[16] R. Guido, T. Mikolajick, U. Schroeder, and P. D. Lomenzo, Role of defects in the breakdown phenomenon of $Al_{1-x}Sc_xN$: From ferroelectric to filamentary resistive switching, Nano Lett. **23**, 7213 (2023).

[17] F. Tasnádi, B. Alling, C. Höglund, G. Wingqvist, J. Birch, L. Hultman, and I. A. Abrikosov, Origin of the anomalous piezoelectric response in wurtzite $Sc_xAl_{1-x}N$ alloys, Phys. Rev. Lett. **104**, 137601 (2010).

[18] S. Zhang, D. Holec, W. Y. Fu, C. J. Humphreys, and M. A. Moram, Tunable optoelectronic and ferroelectric properties in Sc-based III-nitrides, J. Appl. Phys. **114**, 133510 (2013).

[19] K. R. Talley, S. L. Millican, J. Mangum, S. Siol, C. B. Musgrave, B. Gorman, A. M. Holder, A. Zakutayev, and G. L. Brennecka, Implications of heterostructural alloying for enhanced piezoelectric performance of (Al, Sc)N, Phys. Rev. Mater. **2**, 063802 (2018).

[20] H. Wang, N. Adamski, S. Mu, and C. G. Van de Walle, Piezoelectric effect and polarization switching in $Al_{1-x}Sc_xN$, J. Appl. Phys. **130**, 104101 (2021).

[21] H. Zang, Z. Shi, M. Liu, Y. Jia, K. Jiang, J. Ben, Y. Chen, S. Lv, X. Sun, and D. Li, Tunable piezoelectric and ferroelectric responses of $Al_{1-x}Sc_xN$: The role of atomic arrangement, Sci. China: Phys. Mech. Astron. **66**, 277711 (2023).

[22] T. Hwang, W. Aigner, T. Metzger, A. C. Kummel, and K. Cho, First-principles understanding on the formation of inversion

domain boundaries of wurtzite AlN, AlScN, and GaN, ACS Appl. Electron. Mater. **6**, 3257 (2024).

[23] M. Noor-A-Alam, O. Z. Olszewski, and M. Nolan, Ferroelectricity and large piezoelectric response of AlN/ScN superlattice, ACS Appl. Mater. Interfaces **11**, 20482 (2019).

[24] Z. Jiang, C. Paillard, D. Vanderbilt, H. Xiang, and L. Bellaiche, Designing multifunctionality via assembling dissimilar materials: Epitaxial AlN/ScN superlattices, Phys. Rev. Lett. **123**, 096801 (2019).

[25] Z. Jiang, B. Xu, H. Xiang, and L. Bellaiche, Ultrahigh energy storage density in epitaxial AlN/ScN superlattices, Phys. Rev. Mater. **5**, L072401 (2021).

[26] K. H. Ye, G. Han, I. W. Yeu, C. S. Hwang, and J.-H. Choi, Atomistic understanding of the ferroelectric properties of a wurtzite-structure $(AlN)_n/(ScN)_m$ superlattice, Phys. Status Solidi RRL **15**, 2100009 (2021).

[27] N. Farrer and L. Bellaiche, Properties of hexagonal ScN versus wurtzite GaN and InN, Phys. Rev. B **66**, 201203(R) (2002).

[28] V. Ranjan, L. Bellaiche, and E. J. Walter, Strained hexagonal ScN: A material with unusual structural and optical properties, Phys. Rev. Lett. **90**, 257602 (2003).

[29] D. Damjanovic, Ferroelectric, dielectric and piezoelectric properties of ferroelectric thin films and ceramics, Rep. Prog. Phys. **61**, 1267 (1998).

[30] M. Alexe and D. Hesse, Tip-enhanced photovoltaic effects in bismuth ferrite, Nat. Commun. **2**, 256 (2011).

[31] J. Seidel, L. W. Martin, Q. He, Q. Zhan, Y.-H. Chu, A. Rother, M. E. Hawkridge, P. Maksymovych, P. Yu, M. Gajek, N. Balke, S. V. Kalinin, S. Gemming, F. Wang, G. Catalan, J. F. Scott, N. A. Spaldin, J. Orenstein, and R. Ramesh, Conduction at domain walls in oxide multiferroics, Nat. Mater. **8**, 229 (2009).

[32] S. Farokhipoor and B. Noheda, Conduction through 71° domain walls in $BiFeO_3$ thin films, Phys. Rev. Lett. **107**, 127601 (2011).

[33] Q. He, C.-H. Yeh, J.-C. Yang, G. Singh-Bhalla, C.-W. Liang, P.-W. Chiu, G. Catalan, L. W. Martin, Y.-H. Chu, J. F. Scott, and R. Ramesh, Magnetotransport at domain walls in $BiFeO_3$, Phys. Rev. Lett. **108**, 067203 (2012).

[34] C. Paillard, G. Geneste, L. Bellaiche, and B. Dkhil, Vacancies and holes in bulk and at 180° domain walls in lead titanate, J. Phys.: Condens. Matter **29**, 485707 (2017).

[35] L. Cheng, H. Zhang, R. Xu, K. Co, N. Guiblin, M. Otoničar, C. Paillard, Y. Wang, and B. Dkhil, Dislocations and a domains coupling in $PbTiO_3$ thin films, Appl. Phys. Lett. **123**, 201903 (2023).

[36] G. Catalan, J. Seidel, R. Ramesh, and J. F. Scott, Domain wall nanoelectronics, Rev. Mod. Phys. **84**, 119 (2012).

[37] W. Zhu, J. Hayden, F. He, J.-I. Yang, P. Tipsawat, M. D. Hossain, J.-P. Maria, and S. Trolier-McKinstry, Strongly temperature dependent ferroelectric switching in AlN, $Al_{1-x}Sc_xN$, and $Al_{1-x}B_xN$ thin films, Appl. Phys. Lett. **119**, 062901 (2021).

[38] S. Calderon V, J. Hayden, S. M. Baksa, W. Tzou, S. Trolier-McKinstry, I. Dabo, J.-P. Maria, and E. C. Dickey, Atomic-scale polarization switching in wurtzite ferroelectrics, Science **380**, 1034 (2023).

[39] J. P. Perdew, K. Burke, and M. Ernzerhof, Generalized gradient approximation made simple, Phys. Rev. Lett. **77**, 3865 (1996).

[40] G. Kresse and J. Furthmüller, Efficiency of *ab-initio* total energy calculations for metals and semiconductors using a plane-wave basis set, Comput. Mater. Sci. **6**, 15 (1996).

[41] G. Kresse and J. Furthmüller, Efficient iterative schemes for *ab initio* total-energy calculations using a plane-wave basis set, Phys. Rev. B **54**, 11169 (1996).

[42] P. E. Blöchl, Projector augmented-wave method, Phys. Rev. B **50**, 17953 (1994).

[43] R. J. Zeches, M. D. Rossell, J. X. Zhang, A. J. Hatt, Q. He, C.-H. Yang, A. Kumar, C. H. Wang, A. Melville, C. Adamo, G. Sheng, Y.-H. Chu, J. F. Ihlefeld, R. Erni, C. Ederer, V. Gopalan, L. Q. Chen, D. G. Schlom, N. A. Spaldin, L. W. Martin, and R. Ramesh, A strain-driven morphotropic phase boundary in $BiFeO_3$, Science **326**, 977 (2009).

[44] D. Sando, Y. Yang, E. Bousquet, C. Carrétéro, V. Garcia, S. Fusil, D. Dolfi, A. Barthélémy, Ph. Ghosez, L. Bellaiche, and M. Bibes, Large elasto-optic effect and reversible electrochromism in multiferroic $BiFeO_3$, Nat. Commun. **7**, 10718 (2016).

[45] S. S. Hong, M. Gu, M. Verma, V. Harbola, B. Y. Wang, D. Lu, A. Vailionis, Y. Hikita, R. Pentcheva, J. M. Rondinelli, and H. Y. Hwang, Extreme tensile strain states in $La_{0.7}Ca_{0.3}MnO_3$ membranes, Science **368**, 71 (2020).

[46] See Supplemental Material at http://link.aps.org/supplemental/10.1103/PhysRevB.110.054101 for more details about (i) crystal structures of multidomain, monodomain, rocksalt, and zincblende in 1 × 1 AlN/ScN superlattices; (ii) in-plane stress-strain curves of multidomain and monodomain in the AlN/ScN superlattices; (iii) the relation between P_x and P_y in the $Pmc2_1$ space group corresponding to the symmetry of the multidomain supercell; and (iv) the total energy of 3 × 1 AlN/ScN superlattices, which includes Refs. [47,48,60].

[47] B. Mortazavi, I. S. Novikov, and A. V. Shapeev, A machine-learning-based investigation on the mechanical/failure response and thermal conductivity of semiconducting BC_2N monolayers, Carbon **188**, 431 (2022).

[48] N. Ding, X. Chen, and C.-M. L. Wu, Mechanical properties and failure behaviors of the interface of hybrid graphene/hexagonal boron nitride sheets, Sci. Rep. **6**, 31499 (2016).

[49] E. Han, S. M. Nahid, T. Rakib, G. Nolan, P. F. Ferrari, M. A. Hossain, A. Schleife, S. Nam, E. Ertekin, A. M. van der Zande, and P. Y. Huang, Bend-induced ferroelectric domain walls in α-In_2Se_3, ACS Nano **17**, 7881 (2023).

[50] L. Bellaiche, K. Kunc, and J. M. Besson, Isostructural phase transition in InN wurtzite, Phys. Rev. B **54**, 8945 (1996).

[51] V. Ranjan, S. Bin-Omran, L. Bellaiche, and A. Alsaad, Isostructural phase transitions in GaN/ScN and InN/ScN superlattices, Phys. Rev. B **71**, 195302 (2005).

[52] D. Sando, B. Xu, L. Bellaiche, and V. Nagarajan, A multiferroic on the brink: Uncovering the nuances of strain-induced transitions in $BiFeO_3$, Appl. Phys. Rev. **3**, 011106 (2016).

[53] B. Meyer and D. Vanderbilt, *Ab initio* study of ferroelectric domain walls in $PbTiO_3$, Phys. Rev. B **65**, 104111 (2002).

[54] J. B. Neaton, C. Ederer, U. V. Waghmare, N. A. Spaldin, and K. M. Rabe, First-principles study of spontaneous polarization in multiferroic $BiFeO_3$, Phys. Rev. B **71**, 014113 (2005).

[55] Y. Gu, M. Li, A. N. Morozovska, Y. Wang, E. A. Eliseev, V. Gopalan, and L.-Q. Chen, Flexoelectricity and ferroelectric domain wall structures: Phase-field modeling and DFT calculations, Phys. Rev. B **89**, 174111 (2014).

[56] M. D. Dennis and R. C. Bradt, Thickness of 90° ferroelectric domain walls in (Ba, Pb)TiO_3 single crystals, J. Appl. Phys. **45**, 1931 (1974).

[57] G. Venkat, D. A. Allwood, and T. J. Hayward, Magnetic domain walls: types, processes and applications, J. Phys. D: Appl. Phys. **57**, 063001 (2024).

[58] T. Shimada, Y. Umeno, and T. Kitamura, *Ab initio* study of stress-induced domain switching in $PbTiO_3$, Phys. Rev. B **77**, 094105 (2008).

[59] J. Deschamps, Y. Kai, J. Lem, I. Chaban, A. Lomonosov, A. Anane, S. E. Kooi, K. A. Nelson, and T. Pezeril, Additive laser excitation of giant nonlinear surface acoustic wave pulses, Phys. Rev. Appl. **20**, 044044 (2023).

[60] H. T. Stokes and D. M. Hatch, FINDSYM: program for identifying the space-group symmetry of a crystal, J. Appl. Crystallogr. **38**, 237 (2005).